

# Criticality-Enhanced Quantum Sensing with a Parametric Superconducting Resonator

Guillaume Beaulieu,<sup>1,2</sup> Fabrizio Minganti,<sup>2,3,\*</sup> Simone Frasca,<sup>1,2</sup> Marco Scigliuzzo,<sup>2,4</sup> Simone Felicetti,<sup>5,6</sup> Roberto Di Candia,<sup>7,8</sup> and Pasquale Scarlino<sup>1,2,†</sup>

<sup>1</sup>*Hybrid Quantum Circuits Laboratory (HQC), Institute of Physics,  
École Polytechnique Fédérale de Lausanne (EPFL), 1015 Lausanne, Switzerland*

<sup>2</sup>*Center for Quantum Science and Engineering,  
École Polytechnique Fédérale de Lausanne (EPFL), CH-1015 Lausanne, Switzerland*

<sup>3</sup>*Laboratory of Theoretical Physics of Nanosystems (LTPN), Institute of Physics,  
École Polytechnique Fédérale de Lausanne (EPFL), 1015 Lausanne, Switzerland*

<sup>4</sup>*Laboratory of Photonics and Quantum Measurements (LPQM),  
Institute of Physics, EPFL, CH-1015 Lausanne, Switzerland*

<sup>5</sup>*Institute for Complex Systems, National Research Council (ISC-CNR), Via dei Taurini 19, 00185 Rome, Italy*

<sup>6</sup>*Physics Department, Sapienza University, P.le A. Moro 2, 00185 Rome, Italy*

<sup>7</sup>*Department of Information and Communications Engineering, Aalto University, Espoo 02150, Finland*

<sup>8</sup>*Dipartimento di Fisica, Università degli Studi di Pavia, Via Agostino Bassi 6, I-27100, Pavia, Italy*

(Dated: October 1, 2024)

Quantum metrology, a cornerstone of quantum technologies, exploits entanglement and superposition to achieve higher precision than classical protocols in parameter estimation tasks. When combined with critical phenomena such as phase transitions, the divergence of quantum fluctuations is predicted to enhance the performance of quantum sensors. Here, we implement a critical quantum sensor using a superconducting parametric (i.e., two-photon driven) Kerr resonator. The sensor, a linear resonator terminated by a superconducting quantum interference device, operates near the critical point of a finite-component second-order dissipative phase transition obtained by scaling the system parameters. We analyze the performance of a frequency-estimation protocol and show that quadratic precision scaling with respect to the system size can be achieved with finite values of the Kerr nonlinearity. Since each photon emitted from the cavity carries more information about the parameter to be estimated compared to its classical counterpart, our protocol opens perspectives for faster or more precise metrological protocols. Our results demonstrate that quantum advantage in a sensing protocol can be achieved by exploiting a *finite-component* phase transition.

## I. INTRODUCTION

Quantum technologies can offer significant advantages in metrology and sensing [1]. Critical quantum sensing is a promising approach that exploits the quantum properties of phase transitions to achieve optimal precision scaling [2–8]. Theoretical studies primarily focused on quantum phase transitions [9–15], which occur in closed quantum system at zero temperature when the ground state changes as a function of one of the parameters. The non-commutative nature of Hamiltonian terms triggers the transition. While the transition occurs only in the thermodynamic limit of, e.g., an infinite number of atoms, the expected enhanced sensing properties already manifest when scaling-up the system towards this limit.

Despite critical slowing down, critical quantum sensing protocols can saturate the fundamental precision bounds [16]. Experimentally, quantum critical sensors have been implemented using many-body Rydberg atoms [17] and nuclear magnetic resonance techniques [18].

Beyond their application in quantum computing, communication, and simulation [19], superconducting circuits

have a long-standing history in sensing [20–22]. Superconducting quantum interference devices (SQUIDS) are used as highly-sensitive magnetic field sensors; qubits are employed to determine the amplitude of microwave signals at cryogenic temperature through spectroscopy measurements [23, 24]; complex junction-based architectures have been proposed as magnetic-flux sensors to probe magnetic structures [25, 26], detect axions, and conduct dark matter research [27]. Despite theoretical proposals and some experimental evidence of quantum phase transitions in superconducting devices [28, 29], critical metrological protocols have yet to be implemented in superconducting circuits. A main challenge, both in superconducting and other experimental architectures, remains the presence of classical noise and decoherence [30, 31], making it challenging to scale-up these systems while maintaining the low dissipation rates necessary for observing quantum phase transitions.

Recent theoretical proposals show that critical sensing protocols can also be based on *finite-component* quantum phase transitions [32–38]. Here, the “standard” thermodynamic limit (diverging number of atoms) is replaced by a rescaling of the system parameters (diverging number of excitations). *Finite-component* phase transitions provide a tractable framework for theoretically assessing the properties of *critical sensors* [39–46] and offer a means to implement them with *small-scale* controllable

\* Presently at Alice & Bob, Paris, France

† E-mail: pasquale.scarlino@epfl.ch

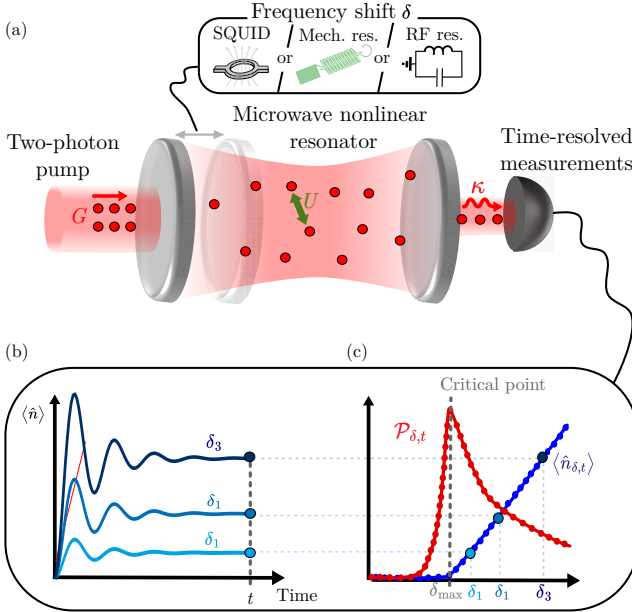


FIG. 1. Sketch of the frequency estimation protocol. (a) A microwave resonator with Kerr nonlinearity  $U$  is driven by a parametric (i.e. two-photon) pump  $G$ . The frequency of the cavity, and consequently the cavity-to-pump detuning  $\delta$ , changes when the cavity length is modified. This system is described by Eqs. (1) and (2). Such frequency tunability can be implemented, for example, using SQUIDs for magnetometry, optomechanical devices for force sensing, and RF resonators longitudinally coupled for MHz signal detection. (b) The cavity field escapes through photon loss at a rate  $\kappa$  and is collected over time by a measurement apparatus, allowing for the reconstruction of the photon number in the cavity  $\langle \hat{n} \rangle$ . (c) From these time traces, the photon number at the steady state  $\langle \hat{n}_{\delta,ss} \rangle$  (blue curve) and the corresponding precision of the estimation of frequency  $\mathcal{P}_{\delta,ss}$  (red curve) are calculated. The maximal precision  $\mathcal{P}_{\delta_{\max},ss}$  is achieved near the critical point of the second-order dissipative finite-component phase transition of the device.

devices [47–53].

Phase transitions [54–58] and their finite-components counterparts [59–62] can also occur in driven-dissipative settings [63, 64], where the steady state of the system, rather than the ground state, undergoes a non-analytical change. In particular, the parametrically (two-photon) driven-dissipative Kerr resonator exhibits first- and second-order dissipative finite-component phase transitions [60, 65], both of which can be explored within a single parametrically-pumped resonator [66, 67]. This type of resonator plays a key role in superconducting quantum technology, such as in Josephson parametric amplifier [68] and cat qubits [69, 70], both of which are built on systems nearly identical to the one considered here. Recent predictions suggest that criticality in the Kerr parametric oscillator could be used to implement optimal critical sensing protocols [46, 71–75], even in the presence of dissipation. Many metrological experiments are lim-

ited by a critical photons (or phonons) number—i.e., a maximal number of excitations that can be present in the sensor before unwanted effects emerge. As a result, maximizing the amount of information extracted per photon becomes pivotal in such experiments, with a key example being the dispersive readout of a superconducting qubit.

In this article, we demonstrate optimal precision scaling with a *finite-component* critical quantum sensor at the steady state. We implement a frequency-estimation protocol with a two-photon driven nonlinear resonator [Fig. 1(a)]. Various platforms could be used to realize such system; in our case, the cavity is implemented with a superconducting resonator that is made both nonlinear and frequency-tunable by incorporating a SQUID. We assess the metrological performance of the device by conducting time resolved measurements of the emission from the cavity [Fig. 1(b)] for various cavity-to-pump detuning. From these measurements, we show that the optimal precision on the frequency estimation is obtained near the critical point of the second-order driven-dissipative phase transition [Fig. 1(c)]. Additionally, by rescaling the system parameters, we demonstrate a quadratic scaling of the estimation precision with respect to the effective system size. We compare this result with the scaling of an optimal classical benchmark, which is theoretically proven to be at best linear with the system size. From a fundamental standpoint, the observed quadratic scaling is a direct signature of the quantum nature of the transition. From an applied perspective, this experiment serves as a proof of concept for the practical relevance of critical quantum sensing in solid-state quantum technologies.

## II. DEVICE AND MODEL

The device is a superconducting  $\lambda/4$  cavity, made nonlinear by a SQUID shunting one end of the cavity to the ground [76]. A coherent tone, sent to a waveguide inductively coupled to the SQUID, generates an oscillating magnetic flux at nearly twice the cavity's resonance frequency [77–79]. This modulation results in a two-photon, or parametric, drive. A coil placed beneath the sample is used to apply a constant flux bias, enabling the tuning of the SQUID's inductance. Tuning the inductance allows to change both the resonance frequency and the nonlinearity of the cavity. Further details can be found in Ref. [66] and Appendix A.

This system is described by the Hamiltonian [66]

$$\hat{H}/\hbar = \delta \hat{a}^\dagger \hat{a} + U/2 \hat{a}^\dagger \hat{a}^\dagger \hat{a} \hat{a} + G/2 (\hat{a}^\dagger \hat{a}^\dagger + \hat{a} \hat{a}), \quad (1)$$

where  $\hat{a}$  is the photon annihilation operator,  $\delta = \omega_r - \omega_p/2$  is the cavity-to-pump detuning [76],  $U$  is the Kerr nonlinearity, and  $G$  is the two-photon drive field amplitude. Throughout the paper, we will study several values of  $U$  and  $G$  while sweeping  $\delta$ . The parametric signal emitted from the cavity is collected through a feedline coupled to the resonator on the opposite side of the SQUID, then filtered and amplified. The interaction of the system with

the feedline, fluxline, and other uncontrolled bath degrees of freedom, is captured by the Lindblad master equation

$$\frac{\partial \rho}{\partial t} = -\frac{i}{\hbar} [\hat{H}, \rho] + \kappa \frac{2\hat{a}\rho\hat{a}^\dagger - \{\hat{a}^\dagger\hat{a}, \rho\}}{2}, \quad (2)$$

where the rate  $\kappa$  is associated with the total photon loss. The total photon loss  $\kappa = \kappa_{\text{int}} + 2\kappa_{\text{ext}}$  is the sum of the intrinsic losses  $\kappa_{\text{int}}$  and the coupling to each direction of the feedline  $\kappa_{\text{ext}}$ , where we assumed the right- and left-coupling to be identical. In the hanger and over-coupled configuration considered here,  $2\kappa_{\text{ext}} \simeq \kappa$ . Other sources of noise are two-photon dissipation, dephasing, and thermal heating, which we find negligible compared to  $\kappa/2\pi \simeq 72 \text{ kHz}$  [66] (c.f. Appendix A 3). As the system evolves, it will eventually reach its steady state  $\rho_{\text{ss}}$  defined by  $\partial_t \rho_{\text{ss}} = 0$ .

The system phases [60, 65, 66] and its sensing capability [73] can be characterized by the average intracavity photon number and its variance. Experimentally, we do not have direct access to these quantities. Instead, we monitor the output field of the cavity over time, after amplification with an effective gain  $G$ . From input-output relations, the measured output field is described by the bosonic output mode  $\hat{A}_{\delta,t} = \sqrt{G}[\sqrt{\kappa_{\text{ext}}} \hat{a}_{\delta,t} + \hat{a}_{\text{amp},t}^\dagger]$ , where  $\hat{a}_{\delta,t}$  is the intracavity field  $\hat{a}$  in the Heisenberg picture and  $\hat{a}_{\text{amp},t}$  is the amplifier noise mode. The output power is then  $\hat{N}_{\delta,t} = \hat{A}_{\delta,t}^\dagger \hat{A}_{\delta,t}$ . As the amplifier noise is uncorrelated to the photon emission, and it averages to zero, the expectation value  $\langle \hat{N}_{\delta,t} \rangle = G[\langle \hat{n}_{\delta,t} \rangle + n_{\text{amp}}]$ , where  $\langle \hat{n}_{\delta,t} \rangle = \kappa_{\text{ext}} \text{Tr}[\hat{a}^\dagger \hat{a} \rho_{\delta,t}]$  is proportional to the intracavity population and  $n_{\text{amp}}$  is the contribution of the amplifier (see Appendix B 1). Experimentally,  $\langle \hat{n}_{\delta,t} \rangle$ , can be obtained by subtracting the amplified noise  $Gn_{\text{amp}}$  (measurement background) from  $\langle \hat{N}_{\delta,t} \rangle$ . As discussed below, the calibration of gain is not necessary for the metrological protocol discussed here. Therefore,  $\langle \hat{n}_{\delta,t} \rangle$  will always be given in arbitrary units.

As we are investigating the metrological properties of the steady state, most of the measurements presented below focus on the steady-state properties (i.e.  $t = \text{ss}$ ). Consequently, we measure  $\langle \hat{N}_{\delta,t} \rangle$  for  $t \gg 1/\kappa$  at discrete time intervals. To accumulate statistics, we collect all the data from  $t > 15 \mu\text{s} \simeq 7/\kappa$  up to an arbitrary long time, fixed in the experiments at  $T = 69 \mu\text{s}$  (see the Appendix B 1 for details). We then average over  $4 \times 10^5$  or  $8 \times 10^5$  independent time traces, depending on the acquisition rate of  $6.7 \times 10^5$  samples per second or  $4 \times 10^6$  samples per second to obtain  $\langle \hat{N}_{\delta,t} \rangle$ .

### III. SCALING TOWARDS THE THERMODYNAMIC LIMIT

In Fig. 2(a), we show  $\langle \hat{n}_{\delta,\text{ss}} \rangle$  as a function of detuning  $\delta$  for  $G/2\pi \approx 300 \text{ kHz}$  and for various values of  $U$  obtained by tuning the DC flux bias (see the Appendix B). All curves show a transition from (i) a vacuum-like state at

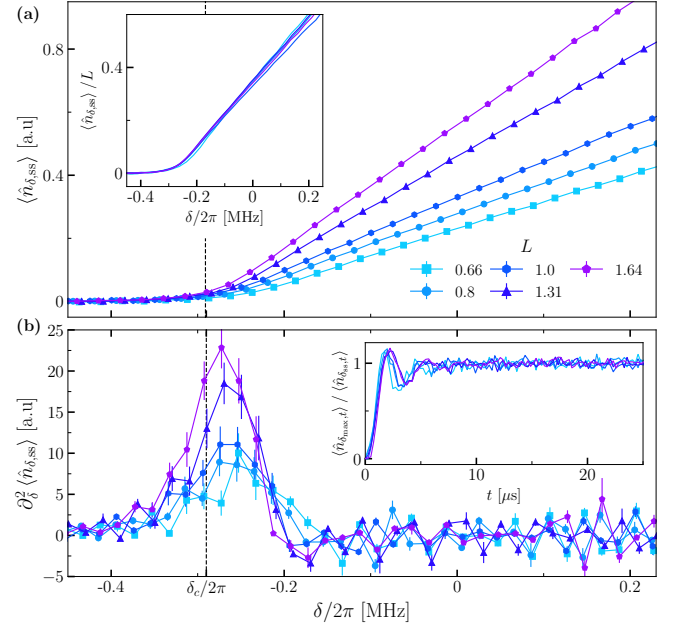


FIG. 2. Signature of the second-order DPT when scaling towards the thermodynamic limit using Scaling (I) in Eq. (3). (a) The expectation value  $\langle \hat{n}_{\delta,\text{ss}} \rangle \propto \text{Tr}[\rho_{\delta,\text{ss}} \hat{a}^\dagger \hat{a}]$  for various  $L$  as a function of the detuning  $\delta$ . The expectation value is obtained by averaging over  $M = 4 \times 10^5$  time traces sampled with an acquisition rate of  $6.7 \times 10^5$  samples per second. The error bars correspond to  $\sqrt{\Delta n_{\delta,\text{ss}}^2 / M}$  where  $\Delta n_{\delta,\text{ss}}$  is the standard deviation over the  $M$  measurements. The inset shows the rescaled photon number  $\langle \hat{n}_{\delta,\text{ss}} \rangle / L$ , demonstrating that all curves collapse onto each other. These data have been obtained by subtracting the amplifier noise  $n_{\text{amp}}$ , as detailed in Appendix B 1. (b) Finite-difference estimation of the second-order derivative  $\partial_\delta^2 \langle \hat{n}_{\delta,\text{ss}} \rangle$ . The error bars are calculated using error-propagation applied to the finite-difference formula. The inset shows the averaged normalized time trace  $\langle \hat{n}_{\delta,\text{ss}} \rangle / \langle \hat{n}_{\delta,\text{ss}} \rangle$ , where  $\delta_{\text{max}}$  corresponds to the peak of  $\partial_\delta^2 \langle \hat{n}_{\delta,\text{ss}} \rangle$ . To capture the fast dynamics, the acquisition rate was set to  $4 \times 10^6$  samples per second for the measurement and the number of averaged traces increased to  $M = 8 \times 10^5$ . Parameters:  $G/2\pi \simeq 300 \text{ kHz}$ ,  $\tilde{U}/2\pi = -9.14 \text{ kHz}$  [where  $U = \tilde{U}/L$ ] and  $\kappa/2\pi \simeq 72 \text{ kHz}$  (details in Appendix B)

$\delta \ll 0$  to (ii) a bright state with a linearly growing number of photons. The passage between (i) and (ii) occurs approximately at  $\delta_c \equiv -\sqrt{G^2 - \kappa^2}$ .

The finite-component system described by Eq. (2) is known to display a second-order DPT in the thermodynamic limit [66]. In this limit, the transition between phases (i) and (ii) remains continuous but becomes non-differentiable. The thermodynamic limit can be reached by one of the following scalings

$$(I) : \quad \delta = \tilde{\delta} \quad G = \tilde{G} \quad U = \tilde{U}/L \quad \kappa = \tilde{\kappa}, \quad (3)$$

$$(II) : \quad \delta = \tilde{\delta}L \quad G = \tilde{G}L \quad U = \tilde{U} \quad \kappa = \tilde{\kappa}L, \quad (4)$$

where the  $\tilde{v}$  indicates the scaled variable associated with

the physical variable  $v$ . Here,  $L$  is a number that plays a role similar to the number of atoms or the lattice size in an extensive system. Scaling towards the thermodynamic limit means considering increasing values of  $L$  and comparing curves with the same  $\tilde{v}$  variables. In the rescaled pictures, curves of  $\langle \hat{n}_{\delta,ss} \rangle / L$  for various  $L$  collapse onto each other. This is shown for the Scaling (I) in the inset of Fig. 2(a). The emergence of the second-order DPT can be seen by calculating  $\partial_{\delta}^2 \langle \hat{n}_{\delta,ss} \rangle$  and comparing curves with the same re-scaled parameters while increasing  $L$ . As shown in Fig. 2(b),  $\partial_{\delta}^2 \langle \hat{n}_{\delta,ss} \rangle$  has a maximum whose value grows with  $L$ , confirming the expected onset of non-analyticity in the thermodynamic limit.

Phase transitions are also characterized by critical slowing down, i.e., the time required for the system to evolve becomes divergently large as the system approaches the thermodynamic limit. In open quantum systems, critical slowing down manifests differently depending on the observables. For instance, observables associated with symmetry breaking at the critical point (such as  $\hat{a}$  in our system) slow down exponentially as  $L$  increases. This was experimentally shown in Ref. [66], with a law  $\langle \hat{a}_t \rangle \propto e^{-\alpha L t}$  with  $\alpha$  a constant of the model. Observables with different symmetry features can, however, follow different dynamics. Specifically, for our system and metrological protocol, the observable of interest is  $\hat{a}^\dagger \hat{a}$ , which is *not* the order parameter associated with spontaneous symmetry breaking. In the inset of Fig. 2(b), we plot the normalized  $\langle \hat{n}_{\delta,ss} \rangle$  as a function of time and for various  $L$ . Despite scaling towards the thermodynamic limit, we observe a negligible difference in the time required to reach the steady state for curves with different  $L$ .

In the following, we focus on the task of measuring a small frequency change  $\delta \rightarrow \delta + \epsilon$ . We will show that the Scaling (I) in Eq. (3) leads to a critically-enhanced scaling of the frequency-estimation precision. In practice, the maximum achievable value of  $L$  is limited by the Kerr nonlinearity. Therefore, we will use the Scaling (II) in Eq. (4) as a proof-of-concept demonstration for precision scaling with larger values of  $L$ , keeping in mind that this also implies a scaling of the estimated parameter itself.

#### IV. ENHANCED SENSING

Given a measurement of  $\hat{N}_{\delta,t}$ , the error in the estimation of  $\delta$  depends on  $\langle \hat{N}_{\delta,t} \rangle$  and on the standard deviation  $\Delta N_{\delta,t} = \sqrt{\langle \hat{N}_{\delta,t}^2 \rangle - \langle \hat{N}_{\delta,t} \rangle^2}$ . The error in the estimation can be characterized by the error propagation formula

$$\Delta \delta_{ss} = \frac{\Delta N_{\delta,ss}}{\left| \partial_{\delta} \langle \hat{N}_{\delta,ss} \rangle \right|} \simeq \frac{(\Delta N_{\delta,ss} + \Delta N_{\delta+\epsilon,ss}) \epsilon}{2 \left| \langle \hat{N}_{\delta,ss} \rangle - \langle \hat{N}_{\delta+\epsilon,ss} \rangle \right|}, \quad (5)$$

where the last part represents a discretized version of the error.

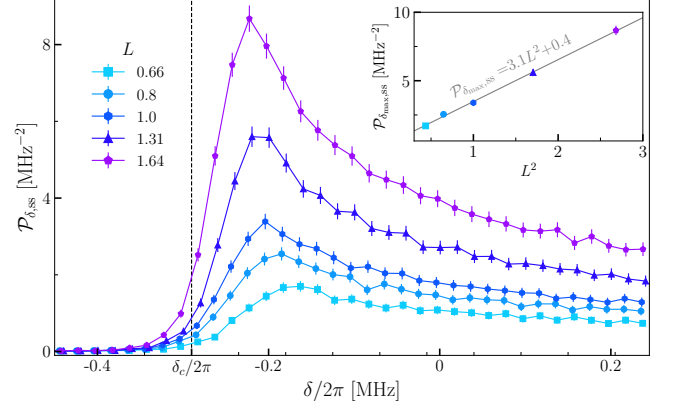


FIG. 3. Precision of the estimation  $\mathcal{P}_{\delta,ss}$  for the Scaling (I) in Eq. (3) calculated as defined in Eq. (5). The error bars are calculated using error-propagation applied to the Eqs. (5) and (6) (see Appendix B 1 for details). The inset shows the maximal precision  $\mathcal{P}_{\delta_{max},ss}$  as a function of  $L$ . The grey line is a fit of the data, demonstrating a quadratic dependence of  $\mathcal{P}_{\delta_{max},ss}$  on  $L$ . Parameters as in Fig. 2(a).

The choice of  $\hat{N}_{\delta,ss}$  implies that the intracavity photon number  $\langle \hat{n}_{\delta,ss} \rangle$  is the resource used to estimate  $\delta$ . Therefore, we expect that the error in the estimation of  $\delta$  will decrease as the photon number increases. Furthermore, Eq. (5) shows that the precision in the estimation of  $\delta$  is independent of any proportionality factor applied to  $\hat{N}_{\delta,ss}$ , making a calibration of the gain value  $\mathcal{G}$  unnecessary. Note, however, that the error is *not* independent on  $n_{amp}$  and increases as  $n_{amp}$  does. Since  $\langle \hat{n}_{\delta,ss} \rangle \propto L$  [see the inset of Fig. 2(a)], we introduce the precision of the estimation  $\mathcal{P}_{\delta,ss}$  of  $\delta$

$$\mathcal{P}_{\delta,ss} = (\Delta \delta_{ss})^{-2} \propto L^{\beta}. \quad (6)$$

where  $\beta = 1 [= 2]$  is an upper bound for a classical [quantum] resource. In Fig. 3, we plot  $\mathcal{P}_{\delta,ss}$  for various values of  $L$ . We remark that by increasing  $L$ , the estimation becomes more precise. Each curve displays a maximum, occurring at  $\delta_{max}$ . In the inset, we observe a quadratic dependence between the maximum of the precision and  $L$ .

#### A. Connecting criticality and enhanced sensing

In the device used for this study, the Kerr nonlinearity can be tuned via the flux bias between  $-13.86$  kHz  $\leq U/2\pi \leq -5.58$  kHz, corresponding to  $0.66 \leq L \leq 1.64$ . As anticipated above, to explore larger values of  $L$  we resort to the Scaling (II) in Eq. (4). Although we cannot independently scale  $\kappa$  without affecting  $U$ , both  $\delta$  and  $G$  can be controlled by changing the frequency and amplitude of the parametric drive, respectively.

We recall here that, given a set of reduced parameters  $\{\tilde{\delta}, \tilde{G}, \tilde{U}, \tilde{\kappa}\}$  and a given value of  $L$ , the two scalings in Eqs. (3) and (4) lead to different physical parameters. It

is, however, meaningful to compare the results for the same rescaled parameters. Namely, we should compare  $\langle \hat{n}_{\delta,ss} \rangle$  vs  $\delta$  for Scaling (I) and  $\langle \hat{n}_{\tilde{\delta},ss} \rangle$  vs  $\tilde{\delta}$  for Scaling (II). Similarly,  $\mathcal{P}_{\delta,ss} = \mathcal{P}_{\tilde{\delta},ss}$  for Scaling (I) and  $\mathcal{P}_{\tilde{\delta},ss} = \mathcal{P}_{\delta/L,ss}$  for Scaling (II). In supplementary Fig. 9, we verify that the two scalings lead to similar results both for the photon number and the precision upon the appropriate rescaling. The overlap of curves with identical values of  $L$ , but different scaling indicates that the Scaling (II) can be used to qualitatively explore larger values of  $L$  that cannot be reached in our device using the Scaling (I).

Therefore, we analyze the metrological properties of the device for larger values of  $L$  for the Scaling (II). In Fig. 4(a), we plot the output photon number at the steady state,  $\langle \hat{n}_{\tilde{\delta},ss} \rangle$ , observing the characteristics indicative of the onset of a second-order DPT. In Fig. 4(b) we plot  $\mathcal{P}_{\tilde{\delta},ss}$  and confirm that the system gains in precision as it scales towards the thermodynamic limit. Figure 4(c) shows the maximum of  $\mathcal{P}_{\tilde{\delta}_{max,ss}}$  as function of  $L$ ; the data are in line with a quadratic scaling, comparable to that observed in Fig. 3. In the same panel, we also plot  $\mathcal{P}_{\tilde{\delta}_{i,ss}}$  for  $\tilde{\delta}_i/2\pi = -0.23$  MHz and  $\tilde{\delta}_i/2\pi = -0.13$  MHz, highlighting the fact that the optimal scaling is achieved around the optimal point  $\tilde{\delta}_{max}$ . Finally, in Fig. 4(d) we show that as  $L$  increases, the difference between the critical point  $\tilde{\delta}_c$  and the point of maximal precision  $\tilde{\delta}_{max}$  decreases, suggesting that the two will eventually coincide for large enough  $L$ . These data show the enhanced sensing capabilities of the parametrically driven Kerr resonator, and that this enhanced sensing occurs near the critical point.

## V. DISCUSSION AND CONCLUSION

In classical pump-and-probe experiments, doubling the pump power does not result in twice the precision. More formally, as shown in the Appendix C, it can be demonstrated that a protocol based on a linear resonator driven by a coherent drive achieves a maximal precision bounded by  $\mathcal{P}_{\delta_{max,ss}} \propto \langle \hat{a}^\dagger \hat{a} \rangle$ , the number of photon in the resonator, even when optimizing over all system and drive parameters. This remains true even in the absence of any noise, internal dissipation or decoherence.

Our experiment is still pump-and-probe, but we have observed a quadratic scaling of the parameter-estimation precision,  $\mathcal{P}_{\delta_{max,ss}} \propto L^2 \propto \langle \hat{a}^\dagger \hat{a} \rangle^2$ . The key difference is that the system is operated in the vicinity of the critical point of a second-order dissipative phase transition. The system's nonlinearity and the parametric quantum process that converts the external drive into a two-photon pump make it possible to overcome the classical precision bound. From a fundamental perspective, our experiment demonstrates that quantum sensing protocols are a valuable tool for characterizing the quantum nature of driven-dissipative phase transitions. Technologically, our results pave the way to the development of a new gen-

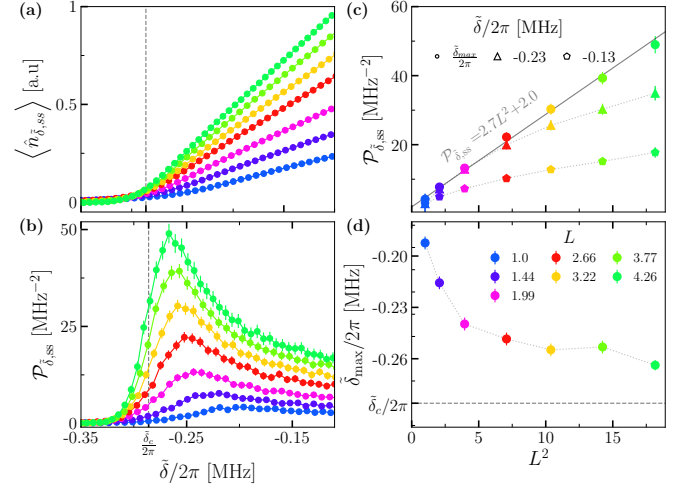


FIG. 4. For the Scaling II in Eq. (4): (a) Output photon number at the steady state  $\langle \hat{n}_{\tilde{\delta},ss} \rangle$  vs scaled detuning  $\tilde{\delta}$  for increasing  $L$ . (b) Precision  $\mathcal{P}_{\tilde{\delta},ss}$  as a function of  $\tilde{\delta}$ . The scaling of  $\mathcal{P}_{\tilde{\delta},ss}$  as a function of  $L$  for various points, including the optimal point  $\tilde{\delta}_{max}$  for each  $L$ . (c)  $\mathcal{P}_{\tilde{\delta}_{max,ss}}$  for  $\tilde{\delta}_i = \tilde{\delta}_{max}$ ,  $\tilde{\delta}_i/2\pi = -0.23$  MHz and  $\tilde{\delta}_i/2\pi = -0.13$  MHz. The solid grey line is a fit of the data demonstrating quadratic dependence for  $\mathcal{P}_{\tilde{\delta}_{max,ss}}$ , while the two light grey dotted lines linking the markers are included as visual guide. (d)  $\tilde{\delta}_{max}$  as a function of  $L$ . The light grey dotted line linking the markers is included as visual guide. Error bars are calculated as in Figs. 2(a) and 3. The error bar in panel (c) corresponds to the size of a detuning step.

eration of quantum sensors based on solid-state critical systems. By selecting an appropriate frequency-tunable component, our frequency estimation protocol could be implemented to sense various quantities, such as magnetic fields using a superconducting quantum interference device (SQUID), forces with an optomechanical devices and a MHz signals with longitudinally coupled RF resonators.

## ACKNOWLEDGMENTS

The authors thank R. Puig I Valls, L. Peyruchat, A. Mercurio, and V. Savona for useful discussions, and V. Jouanny, F. Oppiger and F. De Palma for helping with the measurement setup. S.Fr. acknowledges the support of the Swiss National Science Foundation through the Spark project No. 221051. M.S. acknowledges support from the EPFL Center for Quantum Science and Engineering postdoctoral fellowship. S.Fe. acknowledges financial support from PNRR MUR project PE0000023-NQSTI financed by the European Union – Next Generation EU. R.D. acknowledges support from the Academy of Finland, grants no. 353832 and 349199. P.S. acknowledges support from the Swiss National Science Foundation through Projects No. 206021\_205335 and from the

SERI through grant 101042765\_SEFRI MB22.00081 and Swiss National Science Foundation project UeM019-16 - 215928.

## Appendix A: Device and setup

### 1. Design and fabrication

The device consists of a 150 nm thick aluminum layer on a 525  $\mu\text{m}$  thick high-resistivity silicon substrate. It features a coplanar waveguide resonator fabricated by photolithography followed by wet etching. The nonlinear resonator is grounded through two Al/AlO<sub>x</sub>/Al Josephson junctions forming a superconducting quantum interference device (SQUID). The junctions are made by e-beam lithography using a double-evaporation technique. Further details on the fabrication can be found in Ref. [66]. Figure 5 shows an optical micrograph of the sample used in the experiment, with an SEM zoom of the SQUID in the lower left corner.

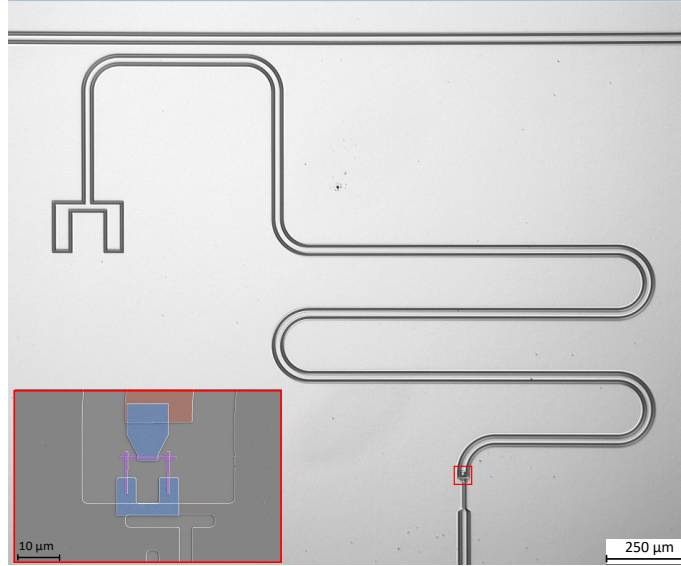


FIG. 5. Optical and SEM images of the device. Micrograph of the device: a  $\lambda/4$  resonator terminated by a SQUID on one end and capacitively coupled to a feedline on the other. In the lower left corner, an SEM of the SQUID, formed by two Josephson junctions (purple), is shown. The SQUID is galvanically connected to the resonator (red) by a patch (blue). The upper part of the fluxline is visible beneath the lower patch. The zoomed-in area corresponds to the red rectangle in the micrograph.

### 2. Experimental setup

The packaged sample is mounted in a high-purity copper enclosure, thermally anchored at the mixing chamber stage of a BlueFors dilution refrigerator. A NbTi coil placed beneath the sample is connected to a current source Yokogawa GS200 to generate a DC flux bias. Two high permeability metal cans provide shielding against external magnetic fields. The cryogenic and room temperature setup is depicted in Fig. 6. An OPX+ and Octave modules generate drives at  $\sim \omega_r$  (single-photon drive for device characterization) and  $\sim 2\omega_r$  (the one which gets converted by three-wave mixing into the two-photon drive). The flux line has 10 dB, 20 dB, and 20 dB attenuators positioned at the 4 K, 800 mK, and 100 mK stages, respectively. The single-photon drive line includes an extra 10 dB attenuator at the mixing chamber stage. Throughout the experiment, the local oscillator used by the Octave to upconvert the signal and used for the single-photon drive remains off to prevent any leakage field in the feedline. It is turned on only before/after the measurements are completed to extract the device parameters. After exiting the Octave, the two pulses are split using a 2-way power divider ZSPD-20180-2S. Half of the signal enters the fridge, while the other half is directed to a spectrum analyzer (Signal Hound USB-SA124B) to monitor the drive amplitude and compensate for any drift. The output signal, collected via the feedline, passes through two circulators (LNF 4-8 GHz Dual Junction Circulator) and travels in a NbTi low-loss superconducting line before being amplified by a 4-8 GHZ LNF High-Electron-Mobility Transistor (HEMT) at the 4K plate. The output signal is further amplified at room temperature using a low noise amplifier (Agile AMT-A0284) before being demodulated in the Octave and digitized in the OPX+.

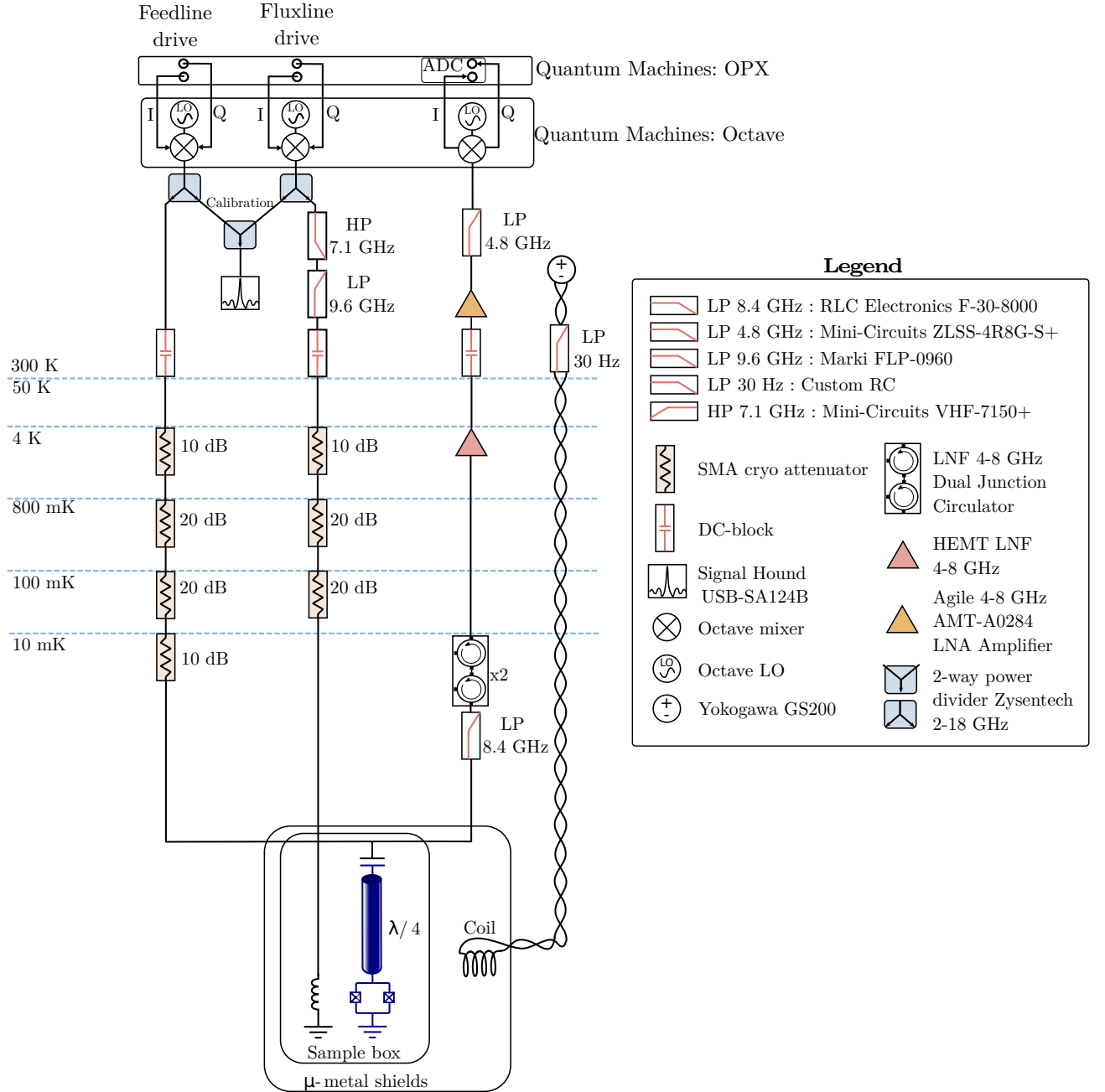


FIG. 6. Schematic of the experimental setup. A two-photon drive is generated by applying a signal to the flux line, which modulates the magnetic flux in the SQUID at frequency  $\omega_p \sim 2\omega_r$ . This parametric excitation of the cavity leads to emission of a signal at  $\omega_p/2$ . The emitted signal is then amplified and filtered to eliminate any component at  $\omega_p$ . The output signal is downconverted to an intermediate frequency to acquire the two quadratures  $I$  and  $Q$ . These intermediate frequency signals are then digitally demodulated and integrated within the OPX + over a time interval  $\Delta T$ , producing a single pair of  $I$  and  $Q$  values.

### 3. Characterization of the device parameters

Circuit quantization of a distributed  $\lambda/4$  resonator terminated by a SQUID allows us to calculate key parameters of the system, i.e.  $\omega_r$  and  $U$ , based on the distributed circuit characteristics. The complete quantization procedure is detailed in Refs. [80–82]. Here, we summarize some of the key results.

The wavevector of the fundamental mode  $k_0$  can be calculated from the transcendental equation

$$\frac{L_{cav}}{L_J} - \frac{C_J(k_0 d)^2}{C_{cav}} = k_0 d \tan(k_0 d), \quad (\text{A1})$$

where  $L_{cav}$  is the inductance of the resonator,  $L_J$  and  $C_J$  are respectively the inductance and capacitance of the SQUID and  $d$  is the length of the resonator. Expressed in terms of resonance frequency and in the limit of small participation ratio  $\gamma = \frac{L_J}{L_{cav}}$ , Eq. (A1) can be rewritten as

$$\omega_0 \approx \frac{\omega_{\lambda/4}}{1 + \gamma}, \quad (\text{A2})$$

where  $\omega_{\lambda/4}$  is the resonance frequency of the fundamental mode of the bare cavity for  $L_J = 0$ . Note that  $\gamma$  varies with the external flux, since the SQUID inductance changes according to  $L_J = \frac{L_J(F=0)}{|\cos(F)|}$ , where  $F = \pi\Phi_{dc}/\Phi_0$ , with  $\Phi_{dc}$  being the DC flux bias and  $\Phi_0$  the flux quantum. We use Eq. (A2) to fit the measured resonance frequency as a function of flux, which allows us to extract  $\gamma$  and  $\omega_{\lambda/4}$ . The magnetic flux is varied by adjusting the current sent to the coil underneath the sample. The result of this measurement is shown by the red datapoints in Fig. 7(a) and the fit by the black line. From the fit, we find the participation ratio  $\gamma = 3.1 \times 10^{-2}$  and the bare cavity frequency  $\omega_{\lambda/4}/2\pi = 4.5068$  GHz. Knowing  $\gamma$  and  $\omega_{\lambda/4}$ , we can calculate the Kerr nonlinearity at different flux points using

$$U = -\frac{\hbar\omega_0^2 L_{cav}}{2\gamma\phi_0^2} \left[ \frac{\cos^2(k_0 d)}{(k_0 d)^2 M_0} \right]^2, \quad (\text{A3})$$

where,

$$M_0 = \left[ 1 + \frac{\sin(2k_0 d)}{2k_0 d} + \frac{2C_J}{C_{cav}} \cos^2(k_0 d) \right]. \quad (\text{A4})$$

The value of  $F$  and  $U$  for the different operating points are reported in Tables. I and II.

Furthermore, for each operating point, the resonance frequency  $\omega_r$  and the coupling to the environment  $\kappa$  are determined by fitting the scattering response  $S_{21}$ . The scattering response is measured by spectroscopy using the feedline (see Fig. 6). For small probe signal amplitude, the scattering coefficient of the hanger resonator can be expressed as [83]

$$S_{21}(f) = ae^{i\alpha} e^{-2\pi i f \tau} \left[ 1 - \frac{(Q_l / |Q_c|)e^{i\phi}}{1 + 2iQ_l(f/f_r - 1)} \right], \quad (\text{A5})$$

where  $f$  is the probe frequency,  $f_r$  is the resonance frequency,  $Q_l$  and  $|Q_c|$  are respectively the loaded and absolute value of the coupling quality factor, and  $\phi$  quantifies the impedance mismatch. The fit is performed using the algorithm provided in [83]. The red markers in Fig. 7(b) show the measured real and imaginary parts of the normalized scattering response  $\tilde{S}_{21} = S_{21}/ae^{j\alpha} e^{-2\pi i f \tau}$ , while the black line corresponds to the fit. From the fit, we obtain resonance frequency  $\omega_r = 2\pi f_r$  and the external coupling  $\kappa = \omega_r/Q_l$ . The values are also reported in Table. (I).

The final parameter to be estimated is the amplitude of the two-photon pump  $G$  at the device. To estimate  $G$ , we use the measurement of the steady state photon number  $\langle \hat{n}_{\delta,ss} \rangle$  as a function of the detuning  $\delta$ . In the mean-field approximation, the stable solution for  $\langle \hat{n}_{ss,\delta} \rangle$  is given by

$$\langle \hat{n}_{\delta,ss} \rangle \approx \frac{\delta + \sqrt{|G|^2 - \kappa^2}}{|U|} \quad (\text{A6})$$

Note that Eq. (A6) assumes a two-photon dissipation rate  $\kappa_2$  and dephasing rate  $\kappa_\phi$  that are much smaller than  $\kappa$ . This assumption holds in our case. In [66], we have estimated the different rates to be of the order  $\kappa_\phi/2\pi \approx 4$  kHz,  $\kappa_2/2\pi \approx 80$  Hz and  $\kappa/2\pi \approx 70$  kHz. In this regime, we can find the value of  $G$  by extrapolating  $\langle \hat{n}_{\delta,ss} \rangle$  to the x-intercept, denoted as  $\delta_0$  [ $\langle \hat{n}_{\delta_0,ss} \rangle = 0$ ] even without knowing the Kerr nonlinearity. The value of  $G$  is then given by

$$G = \sqrt{\delta_0^2 + \kappa^2} \quad (\text{A7})$$

In Fig. 8, we show the measurement of  $\langle \hat{n}_{ss,\delta} \rangle$  as a function of  $\delta$  for Scaling (I) (different values of  $U$ ). The experimental data are shown by markers while the solid lines correspond to a linear fit. By extrapolating the fit to  $\langle \hat{n}_{\delta_0,ss} \rangle = 0$ , we observe that all curves cross at a detuning  $\delta_0$ , indicating that the value of  $G/2\pi = 300$  kHz is consistent across all curves.

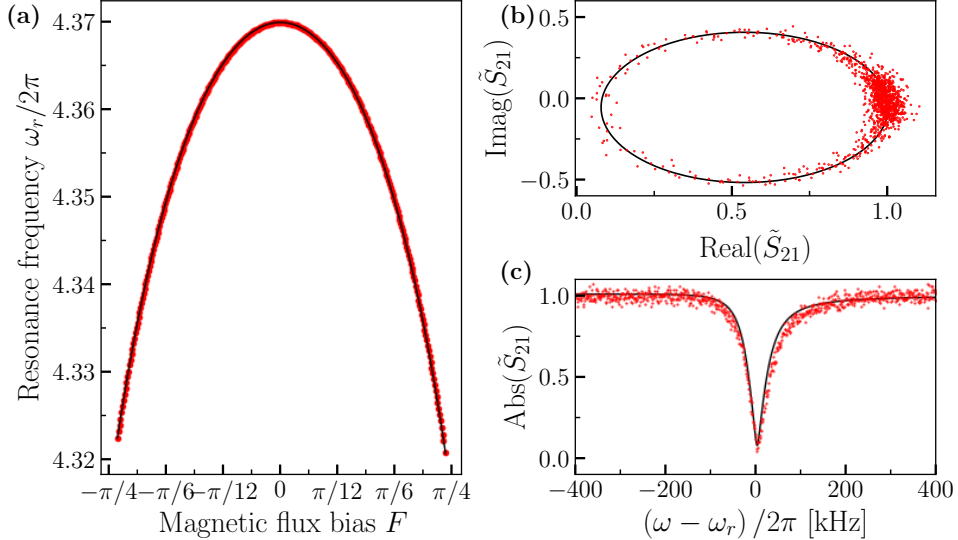


FIG. 7. Measurement of the device parameters. (a) Resonance frequency  $\omega_r$  for varying magnetic flux bias  $F$ . (b) Real against imaginary part of the measured normalized scattering coefficient  $\tilde{S}_{21} = S_{21}/ae^{j\alpha}e^{-2\pi f\tau}$ . (c) The absolute value of the measured normalized scattering coefficient. In all panels, the red markers are the measurements, while the black line indicates the fit to Eq. (A2) for panel (a) and Eq. (A5) for panels (b) and (c).

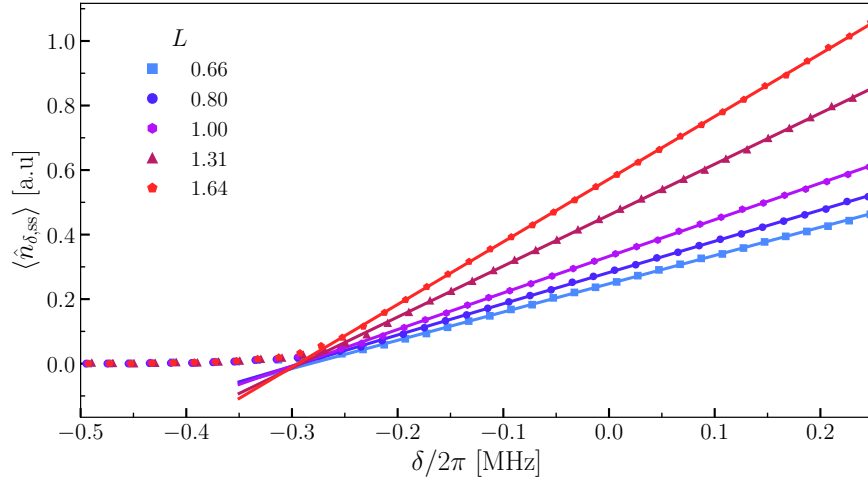


FIG. 8. Estimation of the two-photon pump  $G$ . Markers indicate the expectation value  $\langle \hat{n}_{\delta,ss} \rangle$  for the various  $L$  as a function of the detuning  $\delta$ . The solid lines corresponds to a linear fit. Extrapolation of the linear fit to  $\langle \hat{n}_{\delta_0,ss} \rangle = 0$  allows to estimate the value of  $G$  using Eq. (A7).

## Appendix B: Implementation of the scalings and precision calculation

As detailed in the main text, the Scaling (I) is characterized by the following transformations :

$$(I) : \quad \delta = \tilde{\delta} \quad G = \tilde{G} \quad U = \tilde{U}/L \quad \kappa = \tilde{\kappa}. \quad (\text{B1})$$

To perform this scaling, it is necessary to change only the value of  $U$  while keeping all other parameters fixed. The value of  $U$  is adjusted by varying the external flux  $F$  as described by Eq. (A3). Changing the value of  $F$  will also change the value of  $\omega_r$  as described by Eq. (A2). This can be compensated by modifying the pump frequency  $\omega_p$  to maintain a constant detuning. Table I summarizes the different operating points and the parameters used to realize the Scaling (I). In this table, the value of  $\omega_r$  and  $\kappa$  are obtained by fitting the scattering coefficient  $S_{21}$ . The value of  $U$  and  $F$  are derived from Eq. (A2) and Eq. (A3), respectively. The value of  $G$  is determined by extrapolating  $\langle \hat{n}_{\delta,ss} \rangle$

to the x-intercept as described by Eq. (A7). The pump frequency is set experimentally, and the detuning is defined as  $\delta = \omega_r - \omega_p/2$ . Finally, the value of  $L$  is simply defined from the scaling on the Kerr nonlinearity  $U$ .

TABLE I. Operating points and parameters used for Scaling (I)

$F$	$\omega_r/2\pi$ [GHz]	$\omega_p/2\pi$ [GHz]	$\delta/2\pi$ [MHz]	$U/2\pi$ [kHz]	$L$	$\kappa/2\pi$ [kHz]	$G/2\pi$ [kHz]
0.35	4.361407	8.722320 to 8.723800	-0.5 to 0.25	-5.58	1.64	70	302
0.52	4.349487	8.698474 to 8.699954	-0.5 to 0.25	-7.00	1.31	69	300
0.66	4.334886	8.669280 to 8.670760	-0.5 to 0.25	-9.14	1	70	302
0.75	4.321900	8.643310 to 8.644790	-0.5 to 0.25	-11.36	0.80	75	301
0.82	4.309052	8.617610 to 8.619090	-0.5 to 0.25	-13.38	0.66	76	293

For the Scaling (II), we want to apply the following transformation:

$$(II) : \quad \delta = \tilde{\delta}L \quad G = \tilde{G}L \quad U = \tilde{U} \quad \kappa = \tilde{\kappa}L. \quad (B2)$$

In this case, the Kerr nonlinearity  $U$  remains fixed, while the detuning  $\delta$  and the two-photon pump  $G$  scale with the value of  $L$ . The Scaling (II) is implemented by fixing the external flux  $F$  to 0.66, ensuring that  $U$  and  $\omega_r$  remain constant. Then, the two-photon pump  $G$  is progressively increased, with its value determined by extrapolating  $\langle \hat{n}_{\delta,ss} \rangle$  to the x-intercept. The scaling of  $G$  fixes the value of  $L$ . Finally, knowing  $L$ , the pump frequency  $\omega_p$  is adjusted to maintain the scaling relation. Table II summarizes the different operating points and the parameters used to realize the Scaling (II).

TABLE II. Operating points and parameters used for Scaling (II)

$F$	$\omega_r/2\pi$ [GHz]	$\omega_p/2\pi$ [GHz]	$\delta/2\pi$ [MHz]	$U/2\pi$ [kHz]	$L$	$\kappa/2\pi$ [kHz]	$G/2\pi$ [kHz]
0.66	4.334898	8.670002 to 8.670557	-0.1 to -0.38	-9.14	1	70	291
0.66	4.334893	8.670084 to 8.670881	-0.15 to -0.55	-9.14	1.44	70	428
0.66	4.334891	8.670193 to 8.671309	-0.21 to -0.76	-9.14	1.99	70	594
0.66	4.334896	8.670316 to 8.671791	-0.26 to -1.00	-9.14	2.66	70	796
0.66	4.334895	8.670421 to 8.672202	-0.32 to -1.21	-9.14	3.22	70	965
0.66	4.334896	8.670523 to 8.672600	-0.37 to -1.40	-9.14	3.77	70	1130
0.66	4.334896	8.670617 to 8.673000	-0.31 to -1.60	-9.14	4.26	70	1278

The equivalence of the two scaling is demonstrated in Fig. 9. In Fig. 9 (a), we compare  $\langle \hat{n}_{\delta,ss} \rangle$  vs  $\delta$  for scaling (I) and  $\langle \hat{n}_{\tilde{\delta},ss} \rangle$  vs  $\tilde{\delta}$  for scaling (II). Similarly in Fig. 9 (b),  $\mathcal{P}_{\delta,ss} = \mathcal{P}_{\delta,ss}$  for Scaling (I) and  $\mathcal{P}_{\tilde{\delta},ss} = \mathcal{P}_{\delta/L,ss}$  for Scaling (II). We see that both scalings lead to similar results for both photon number and the precision.

### 1. Precision estimation from the measured data

After determining the parameters ( $G$ ,  $F$ , and  $\omega$ ), we proceed with the measurements. For each measurement, the pump  $G$  is turned on at a fixed frequency  $\omega_p$  and we measure a trajectory by continuously acquiring the signal quadratures  $\hat{I}$  and  $\hat{Q}$  for a total time  $T = 69\text{ }\mu\text{s}$ . Each quadrature is integrated for a time  $\Delta T$  of  $1.5\text{ }\mu\text{s}$  for all the steady state measurements (Figs. 2, 3, 4 and 9) and  $250\text{ ns}$  for the dynamical measurement [inset of Fig. 2(b)]. Mathematically, we define

$$\hat{I}_j = \frac{1}{\Delta T} \int_{t_j}^{t_j + \Delta T} d\tau \sqrt{\mathcal{G}} [\hat{i}(\tau) + \hat{\mu}(\tau)] \quad (t_{j+1} = t_j + \Delta T) \quad (j = 1, \dots, J) \quad (B3)$$

$$\hat{Q}_j = \frac{1}{\Delta T} \int_{t_j}^{t_j + \Delta T} d\tau \sqrt{\mathcal{G}} [\hat{q}(\tau) + \hat{\nu}(\tau)] \quad (t_{j+1} = t_j + \Delta T) \quad (j = 1, \dots, J) \quad (B4)$$

where  $\mathcal{G}$  represents the effective gain of the output line,  $\hat{\mu}(\tau)$  and  $\hat{\nu}(\tau)$  are the amplifier noise quadratures, and  $\hat{i}(\tau)$  and  $\hat{q}(\tau)$  are the signal quadrature. Notice that  $\hat{I}_j$  and  $\hat{Q}_j$  are incompatible observables. However, they can be

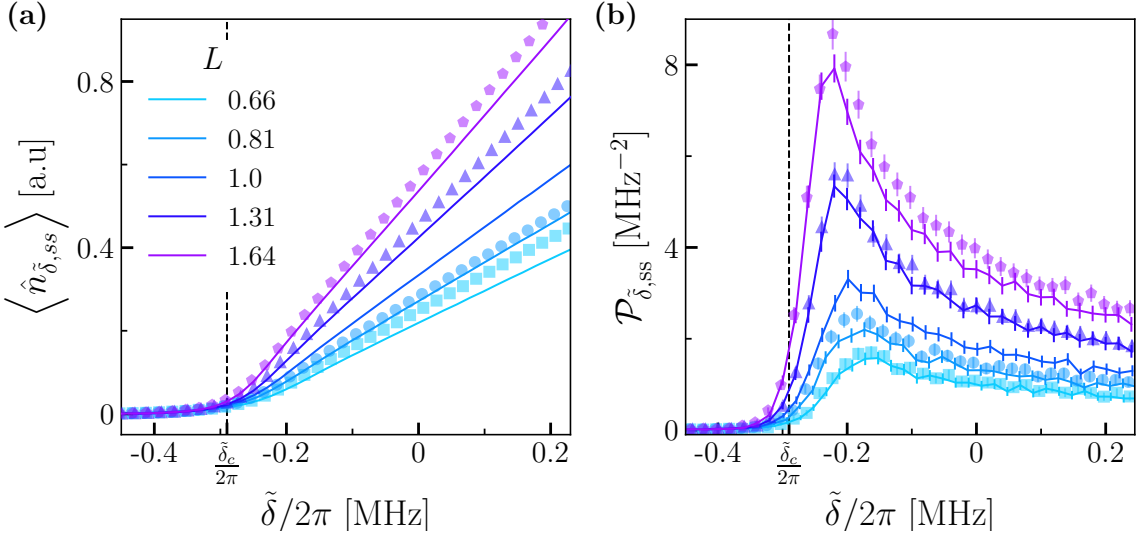


FIG. 9. Comparison between the Scalings I in Eq. (3) and II in Eq. (4) (solid lines) : (a) Output photon number at the steady state vs scaled detuning  $\tilde{\delta}$  for increasing  $L$ . (b) Precision  $P_{\delta,ss}$  as a function of  $\tilde{\delta}$ . Parameters as in Fig. 2.

approximately measured simultaneously in the large  $\mathcal{G}$  limit. The index  $j$  ranges from 1 to  $J = T/\Delta T$  and corresponds to the number of data points acquired in a measurement trace. To simplify the notation, we define the following

$$\hat{i}_j = \frac{1}{\Delta T} \int_{t_j}^{t_j + \Delta T} d\tau \hat{i}(\tau) \quad (\text{B5})$$

$$\hat{q}_j = \frac{1}{\Delta T} \int_{t_j}^{t_j + \Delta T} d\tau \hat{q}(\tau) \quad (\text{B6})$$

$$\hat{\mu}_j = \frac{1}{\Delta T} \int_{t_j}^{t_j + \Delta T} d\tau \hat{\mu}(\tau) \quad (\text{B7})$$

$$\hat{\nu}_j = \frac{1}{\Delta T} \int_{t_j}^{t_j + \Delta T} d\tau \hat{\nu}(\tau). \quad (\text{B8})$$

Using these definitions, the quantity of interest - i.e., the measured output power - is

$$\hat{N}_j = \hat{i}_j^2 + \hat{Q}_j^2 = \mathcal{G} \left[ \hat{i}_j^2 + \hat{q}_j^2 + \hat{\mu}_j^2 + \hat{\nu}_j^2 + 2\hat{\mu}_j \hat{i}_j + 2\hat{\nu}_j \hat{q}_j \right]. \quad (\text{B9})$$

After the single measurement trace has been collected, the pump  $G$  is turned off and we wait 100  $\mu\text{s}$  for the resonator to return to the vacuum state before acquiring the next trace. The precision for estimating the parameter  $\delta$  depends on the first and second moments of  $\langle \hat{N}_j \rangle$  at two different, but close, values of  $\delta$ . The moments are estimated by repeating the measurement  $M = 400 \times 10^3$  times to obtain the set  $\{I_{j,m}, Q_{j,m}\}_{m=1}^M$  of measurement samples. This allows us to estimate the expectation values

$$\langle \hat{N}_j \rangle \approx \frac{1}{M} \sum_{m=1}^M I_{j,m}^2 + Q_{j,m}^2 \quad (\text{B10})$$

$$\langle \hat{N}_j^2 \rangle \approx \frac{1}{M} \sum_{m=1}^M (I_{j,m}^2 + Q_{j,m}^2)^2 \quad (\text{B11})$$

The measurement protocol is repeated for different values of detuning  $\delta$  to obtain  $\langle \hat{N}_{\delta,j} \rangle$  and  $\langle \hat{N}_{\delta,j}^2 \rangle$ . We can then calculate the error on the estimation of  $\delta$  using measurements with nearby detuning values (i.e., separated by a small  $\epsilon$ )

$$\Delta\delta_{\text{ss}} = \frac{\Delta N_{\delta,\text{ss}}}{\left| \partial_\delta \langle \hat{N}_{\delta,\text{ss}} \rangle \right|} \approx \frac{(\Delta N_{\delta,\text{ss}} + \Delta N_{\delta+\epsilon,\text{ss}}) \epsilon}{2 \left| \langle \hat{N}_{\delta,\text{ss}} \rangle - \langle \hat{N}_{\delta+\epsilon,\text{ss}} \rangle \right|} \quad (\text{B12})$$

where  $\Delta N_{\delta,j} = \sqrt{\langle \hat{N}_{\delta,j}^2 \rangle - \langle \hat{N}_{\delta,j} \rangle^2}$ . Finally, the precision of the estimation of  $\delta$  is simply  $\mathcal{P}_{\delta,j} = (\Delta \delta_j)^{-2}$ . The steady state precision is calculated with greater accuracy by averaging over the  $J_{ss}$  values of precisions where the system has reached the steady state. We label the index  $j_{ss}$  as the first index where the system is in the steady state ( $J_{ss} = J - j_{ss}$ )

$$\mathcal{P}_{\delta,ss} = \frac{1}{J_{ss}} \sum_{j=j_{ss}}^J \mathcal{P}_{\delta,j} \quad (B13)$$

We find that the system has well reached the steady state for  $t > 15 \mu s$ , which corresponds to approximately seven times the dissipation rate.

Notice that we can parameterize the expectation value of the output power as  $\langle \hat{N}_j \rangle = \mathcal{G}[\langle \hat{n}_j \rangle + n_{amp}]$ , as done in the main text. We can obtain an estimation of  $\mathcal{G}n_{amp}$  by performing the same type of measurement, but with  $G = 0$ , such that the intracavity state is vacuum. This allows us to obtain  $\langle \hat{n}_j \rangle$  up to the proportionality factor  $\mathcal{G}$  for Figs. 2(a) and 4(a).

## 2. Precision dependence on the amplifier noise

Let us estimate the precision defined Eq. (B12) on the amplifier noise. We model the amplifier noise as white thermal noise with  $\langle \hat{\mu}(\tau)\hat{\mu}(\tau') \rangle = \langle \hat{\nu}(\tau)\hat{\nu}(\tau') \rangle = \sigma^2 \delta(t - t')$  and  $\langle \hat{\mu}(\tau)\hat{\nu}(\tau') \rangle = 0$ , where  $\sigma^2 \geq 1/4$  (we have set the variance of the vacuum quadrature to 1/4). This implies that  $\langle \hat{\mu}_j^2 \rangle = \langle \hat{\nu}_j^2 \rangle = \sigma^2 / \sqrt{\Delta T}$  and  $\langle \hat{\mu}_j \hat{\nu}_j \rangle = 0$ , where  $\Delta T$  is the integration time.

Let us also define the power operators  $\hat{p}_j = \sqrt{\Delta T}(\hat{i}_j^2 + \hat{q}_j^2)$ . We have that

$$\frac{1}{\mathcal{G}} \langle \hat{N}_j \rangle = \langle \hat{i}_j^2 \rangle + \langle \hat{q}_j^2 \rangle + \langle \hat{\mu}_j^2 \rangle + \langle \hat{\nu}_j^2 \rangle = \frac{1}{\sqrt{\Delta T}} [\langle \hat{p}_j \rangle + 2\sigma^2]. \quad (B14)$$

For the second moment, we get

$$\frac{1}{\mathcal{G}^2} \langle \hat{N}_j^2 \rangle = \frac{1}{\Delta T} \langle \hat{p}_j^2 \rangle + \langle (\hat{\mu}_j^2 + \hat{\nu}_j^2)^2 \rangle + 4\langle \hat{\mu}_j^2 \rangle \langle \hat{i}_j^2 \rangle + 4\langle \hat{\nu}_j^2 \rangle \langle \hat{q}_j^2 \rangle + 2\langle \hat{\mu}_j^2 + \hat{\nu}_j^2 \rangle \langle \hat{i}_j^2 + \hat{q}_j^2 \rangle \quad (B15)$$

$$= \frac{1}{\Delta T} \langle \hat{p}_j^2 \rangle + \langle (\hat{\mu}_j^2 + \hat{\nu}_j^2)^2 \rangle + \frac{8\sigma^2}{\Delta T} \langle \hat{p}_j \rangle \quad (B16)$$

$$= \frac{1}{\Delta T} [\langle \hat{p}_j^2 \rangle + 8\sigma^4 - 1/4 + 8\sigma^2 \langle \hat{p}_j \rangle], \quad (B17)$$

where we have used that  $\langle (\hat{\mu}_j^2 + \hat{\nu}_j^2)^2 \rangle = (8\sigma^4 - 1/4)/\Delta T$ . All in all, we obtain

$$\frac{\Delta N_j}{|\partial_\delta \langle \hat{N}_j \rangle|} = \frac{\Delta p_j + 4\sigma^2 \langle \hat{p}_j \rangle + 4\sigma^4 - 1/4}{|\partial_\delta \langle \hat{p}_j \rangle|} = \frac{\Delta p_j}{|\partial_\delta \langle \hat{p}_j \rangle|} \left[ 1 + \frac{4\sigma^2 \langle \hat{p}_j \rangle + 4\sigma^4 - 1/4}{\Delta p_j} \right], \quad (B18)$$

where  $\Delta p_j = \sqrt{\langle \hat{p}_j^2 \rangle - \langle \hat{p}_j \rangle^2}$ . Since  $\langle \hat{p}_j \rangle > 0$  and  $4\sigma^4 - 1/4 \geq 0$ , it is clear that increasing the amplifier noise level  $\sigma^2$  induces a decrease of precision in the metrological protocol.

## 3. Error bars

The error on the estimation of the precision, which we label  $\text{Err}[P_{\delta,j}]$  to simplify the notation, is calculated using the error propagation formula applied to Eq. (B12)

$$\text{Err}[P_{\delta,j}] = 2P_{\delta,j} \sqrt{\frac{\text{Err}[\langle \hat{N}_{\delta,j} \rangle]^2 + \text{Err}[\langle \hat{N}_{\delta+\epsilon,j} \rangle]^2}{\langle \hat{N}_{\delta,j} \rangle - \langle \hat{N}_{\delta+\epsilon,j} \rangle} + \frac{\text{Err}[\Delta N_{\delta,j}]^2 + \text{Err}[\Delta N_{\delta+\epsilon,j}]^2}{(\Delta N_{\delta,j} - \Delta N_{\delta+\epsilon,j})^2} + \frac{\text{Err}[\epsilon]^2}{\epsilon^2}} \quad (B19)$$

where the error on the sample means are given by  $\text{Err}[\langle \hat{N}_{\delta,j} \rangle] = \sqrt{\Delta N_{\delta,j}^2/M}$  and  $\text{Err}[\langle \hat{N}_{\delta+\delta,j} \rangle] = \sqrt{\Delta N_{\delta+\delta,j}^2/M}$ , while the errors on the standard deviations are given by  $\text{Err}[\Delta N_{\delta,j}] = \sqrt{\Delta N_{\delta,j}^2/(2M)}$  and  $\text{Err}[\Delta N_{\delta+\epsilon,j}] = \sqrt{\Delta N_{\delta+\epsilon,j}^2/(2M)}$ . The error in the detuning step  $\epsilon$  comes from fluctuations in the resonator frequency  $\omega_r$ . By continuously monitoring the resonator frequency through spectroscopy measurements, we estimate that the resonator frequency fluctuations over a time duration comparable to the measurement time are at most on the order of 1 kHz. The final error for the steady state value is then taken as

$$\text{Err}[P_{\delta,ss}] = \sqrt{\frac{\left(\frac{1}{J_{ss}} \sum_{j=J_{ss}}^J \text{Err}[P_{\delta,j}] \right)^2}{J_{ss}}} \approx \sqrt{\frac{\text{Err}[P_{\delta,J_{ss}}]^2}{J_{ss}}} \quad (\text{B20})$$

## Appendix C: Classical benchmark

Here, we provide the details about the parameter estimation protocol based on a linear driving. We will demonstrate two facts: (i) The maximal precision for a linear resonator is achieved when a pumping mechanism drives it at resonance; (ii) The precision increases linearly with the number of photons. Using the language of the main text, we deduce that  $P_{\delta_{\max},ss} \propto \langle \hat{a}^\dagger \hat{a} \rangle$ , the photon number in the resonator, with  $\delta_{\max} = 0$ .

### 1. Estimation of the precision with single frequency-resolved measurement

We consider a one-sided resonator driven with a monochromatic coherent input centered around the frequency  $\omega_p$ . In this case, information about the resonator frequency is imparted on the phase of the reflected signal, which is read out through homodyne measurement. Let us define the input field as

$$|\psi_{in}\rangle = \exp\{\alpha^* \hat{m} - \alpha \hat{m}^\dagger\} |0\rangle \equiv \hat{D}_m(\alpha) |0\rangle, \quad (\text{C1})$$

where  $\hat{D}_m(\alpha)$  is a displacement operator of the single mode  $\hat{m}_{in}$ , defined as

$$\hat{m}_{in} = \int d\omega f(\omega) \hat{a}_{in}(\omega), \quad \text{where} \quad \int d\omega f(\omega)^2 = 1. \quad (\text{C2})$$

For the sake of simplicity, we take  $f(\omega) \in \mathbb{R}$ . Using input-output theory we find a linear relationship between the frequency components of the input and output fields,

$$\hat{a}_{out}(\omega) = \frac{\kappa_{\text{ext}}/2 + i(\omega - \omega_r)}{\kappa_{\text{ext}}/2 - i(\omega - \omega_r)} \hat{a}_{in}(\omega) \equiv \Gamma(\omega) \hat{a}_{in}(\omega). \quad (\text{C3})$$

We assume for now that we are able to measure an output mode which has the same profile as the input wavepacket,

$$\hat{m}_{out} \equiv \int d\omega f(\omega) \hat{a}_{out}(\omega) = \int d\omega f(\omega) \Gamma(\omega) \hat{a}_{in}(\omega). \quad (\text{C4})$$

Given that the input is a Gaussian state, we know that the optimal measurement is homodyne. In order to estimate the precision over the estimation of  $\omega_r$ , we need to calculate the first- and second-moments of the readout mode  $\hat{m}_{out}$ .

Using the relation  $\hat{a}_{in}(\omega) \hat{D}_m(\alpha) |0\rangle = \alpha f(\omega) \hat{D}_m(\alpha) |0\rangle$ , we find for the first moment of the output mode

$$\langle \hat{m}_{out} \rangle = \alpha \int d\omega f(\omega)^2 \Gamma(\omega) \approx \alpha \Gamma(\omega_p), \quad (\text{C5})$$

where we have taken the input to be effectively in a monochromatic wavepacket centered around the drive frequency  $\omega_p$ , and with a bandwidth much smaller than the resonator linewidth  $\kappa_{\text{ext}}$  and the drive frequency  $\omega_p$ , that is

$$\int d\omega \omega f(\omega)^2 = \omega_p, \quad \text{and} \quad \sqrt{\int d\omega (\omega^2 - \omega_p^2) f(\omega)^2} \equiv \Delta\omega \ll \kappa_{\text{ext}}, \omega_p. \quad (\text{C6})$$

The condition  $\Delta\omega \ll \omega_p$  is the narrow bandwidth approximation, which allows us to work with integration limits from  $-\infty$  to  $+\infty$ . Similarly, we can calculate the second-order moment of the output mode, as for example:

$$\begin{aligned}\langle \hat{m}_{\text{out}}^\dagger \hat{m}_{\text{out}} \rangle &= \iint d\omega_1 d\omega_2 f(\omega_1) f(\omega_2) \Gamma(\omega_1)^* \Gamma(\omega_2) \langle \hat{a}_{\text{in}}(\omega_1)^\dagger \hat{a}_{\text{in}}(\omega_2) \rangle \\ &= |\alpha|^2 \iint d\omega_1 d\omega_2 f(\omega_1)^2 f(\omega_2)^2 \Gamma(\omega_1)^* \Gamma(\omega_2) = |\alpha|^2 |\Gamma(\omega_p)|^2 = |\alpha|^2.\end{aligned}\quad (\text{C7})$$

We want to estimate  $\omega_r$  from homodyne measurements performed on the output mode  $\hat{m}_{\text{out}}$ . Let us define  $\omega_r = \omega_0 + \delta$ , where  $\omega_0$  is our prior information on the parameter and  $\delta$  is a small shift to be estimated. To simplify the expressions, we define  $\Delta_p = \omega_p - \omega_0$ , as the detuning between the driving and the prior frequency. We then rewrite

$$\Gamma(\omega_p) = \frac{\kappa_{\text{ext}}/2 + i(\omega_p - \omega_r)}{\kappa_{\text{ext}}/2 - i(\omega_p - \omega_r)} = \frac{\kappa_{\text{ext}}/2 + i(\Delta_p - \delta)}{\kappa_{\text{ext}}/2 - i(\Delta_p - \delta)} \equiv \Gamma(\Delta_p). \quad (\text{C8})$$

Notice that since  $|\Gamma(\Delta_p)| = 1$ , then we can rewrite

$$\Gamma(\Delta_p) = \left( \frac{\kappa_{\text{ext}}/2 + i\Delta_p}{\kappa_{\text{ext}}/2 - i\Delta_p} \right) \left( \frac{\kappa_{\text{ext}}^2 - 4\Delta_p\delta + 4\Delta_p^2 - 2i\kappa_{\text{ext}}\delta}{\kappa_{\text{ext}}^2 - 4\Delta_p\delta + 4\Delta_p^2 + 2i\kappa_{\text{ext}}\delta} \right) = e^{i\phi_0} \left[ 1 - \frac{4i\kappa_{\text{ext}}\delta}{\kappa_{\text{ext}}^2 + 4\Delta_p^2} + O(\delta^2) \right], \quad (\text{C9})$$

where  $e^{i\phi_0}$  is a phase, which is independent of the parameter  $\delta$  to be estimated. We have expanded the expression up to the first order in  $\delta$  to make explicit the value of the first-order derivative. This expression helps us identify the phase of the optimal readout quadrature, given by  $\hat{p}_{\text{out}} = (e^{-i\phi_0} \hat{m}_{\text{out}} - e^{i\phi_0} \hat{m}_{\text{out}}^\dagger) / 2i$ .

The precision over the estimation of  $\omega_r$  is then given by the precision of the homodyne signal,

$$\mathcal{P}(\Delta_p) = \frac{[\partial_\delta \langle \hat{p}_{\text{out}}(\phi) \rangle]^2}{\langle \Delta \hat{p}_{\text{out}}(\phi)^2 \rangle}. \quad (\text{C10})$$

As the mode  $\hat{m}_{\text{out}}$  is in a coherent state, we have directly  $\langle \Delta \hat{p}_{\text{out}}(\phi)^2 \rangle \equiv \langle \hat{p}_{\text{out}}(\phi)^2 \rangle - \langle \hat{p}_{\text{out}}(\phi) \rangle^2 = 1/4$ . For the signal we find

$$\langle \hat{p}_{\text{out}}(\phi) \rangle = \frac{\alpha}{2i} [\Gamma(\Delta_p) e^{-i\phi_0} - \Gamma(\Delta_p)^* e^{i\phi_0}] = \alpha \text{Im} \{ \Gamma(\omega_p) e^{-i\phi_0} \} = -\frac{4\kappa_{\text{ext}}}{\kappa_{\text{ext}}^2 + 4\Delta_p^2} \alpha \delta + O(\delta^2). \quad (\text{C11})$$

Inserting this result into Eq. (C10), we finally find

$$\mathcal{P}(\Delta_p) = \frac{64\kappa_{\text{ext}}^2}{(\kappa_{\text{ext}}^2 + 4\Delta_p^2)^2} \alpha^2. \quad (\text{C12})$$

The precision reaches its maximum for  $\Delta_p = 0$ , and is linear in the number of photons of the output field  $\langle \hat{m}_{\text{out}}^\dagger \hat{m}_{\text{out}} \rangle = \alpha^2$ .

## 2. Precision dependence on measurement time and bandwidth

So far, we have assumed that we can measure the output mode  $\hat{m}_{\text{out}}$ . This mode is narrowly peaked in frequency and, accordingly, it has a wide distribution in time. Hence, in deriving Eq. (C12) we have implicitly assumed a long measurement time. In order to calculate the time scaling of the estimation precision, we must define readout modes accessible with a finite measurement time  $T$ ,

$$\hat{A}_{\text{out}} = \frac{1}{\sqrt{T}} \int_t^{t+T} d\tau e^{i\omega_p(\tau-t_0)} \hat{a}_{\text{out}}(\tau), \quad (\text{C13})$$

where  $\hat{a}_{\text{out}}(\tau) = \frac{1}{\sqrt{2\pi}} \int d\omega e^{-i\omega(\tau-t_0)} \hat{a}_{\text{out}}(\omega)$ . Let us calculate the first and second moments of this mode. As frequency distribution of the drive, we consider a narrow square function  $f = \frac{1}{\sqrt{B}} \mathbb{I}[\omega \in (\omega_p - B/2, \omega_p + B/2)]$ . We have that

$$\langle \hat{A}_{\text{out}} \rangle = \frac{1}{\sqrt{T}} \int_t^{t+T} d\tau e^{i\omega_p(\tau-t_0)} \langle \hat{a}_{\text{out}}(\tau) \rangle = \frac{1}{\sqrt{2\pi T}} \int_t^{t+T} d\tau e^{i\omega_p(\tau-t_0)} \int d\omega e^{-i\omega(\tau-t_0)} \langle \hat{a}_{\text{out}}(\omega) \rangle \quad (\text{C14})$$

$$= \frac{1}{\sqrt{2\pi T}} \int_t^{t+T} d\tau e^{i\omega_p(\tau-t_0)} \int d\omega e^{-i\omega(\tau-t_0)} \Gamma(\omega) f(\omega) \alpha \quad (\text{C15})$$

$$\approx \frac{1}{\sqrt{2\pi T}} \int_t^{t+T} d\tau e^{i\omega_p(\tau-t_0)} e^{-i\omega_p(\tau-t_0)} \int_{\omega_p-B/2}^{\omega_p+B/2} d\omega \frac{\Gamma(\omega_p) \alpha}{\sqrt{B}} \quad (\text{C16})$$

$$= \sqrt{\frac{BT}{2\pi}} \Gamma(\omega_p) \alpha. \quad (\text{C17})$$

Similarly, we get that  $N_{\text{out}} = \langle \hat{A}_{\text{out}}^\dagger \hat{A}_{\text{out}} \rangle = BT|\alpha|^2/2\pi$ . Since  $|\langle \hat{A}_{\text{out}} \rangle| = \sqrt{\langle \hat{A}_{\text{out}}^\dagger \hat{A}_{\text{out}} \rangle}$ , where we use that  $|\Gamma(\omega_p)| = 1$ , we conclude that  $\hat{A}_{\text{out}}$  is in a coherent state, and the variance of its quadratures is  $1/4$ . The precision of the optimal observable, which is  $\hat{P}_{\text{out}} = (e^{-i\phi_0} \hat{A}_{\text{out}} - e^{-i\phi_0} \hat{A}_{\text{out}}^\dagger)/2i$ , is

$$\mathcal{P}_{\Delta_p, T} = \frac{64\kappa_{\text{ext}}^2}{(\kappa_{\text{ext}}^2 + 4\Delta_p^2)^2} \frac{BT\alpha^2}{2\pi} = \frac{64\kappa_{\text{ext}}^2}{(\kappa_{\text{ext}}^2 + 4\Delta_p^2)^2} N_{\text{out}}, \quad (\text{C18})$$

which is optimal for  $\Delta_p = 0$ . To conclude, when the input is a monochromatic coherent state and the resonator has no quantum nonlinearity, the optimal scaling of the estimation precision is linear with respect to time and photon number.

- 
- [1] C. L. Degen, F. Reinhard, and P. Cappellaro, Quantum sensing, *Rev. Mod. Phys.* **89**, 035002 (2017).
- [2] P. Zanardi, M. G. A. Paris, and L. Campos Venuti, Quantum criticality as a resource for quantum estimation, *Phys. Rev. A* **78**, 042105 (2008).
- [3] C. Invernizzi, M. Korbman, L. Campos Venuti, and M. G. A. Paris, Optimal quantum estimation in spin systems at criticality, *Phys. Rev. A* **78**, 042106 (2008).
- [4] M. Tsang, Quantum transition-edge detectors, *Phys. Rev. A* **88**, 021801 (2013).
- [5] P. A. Ivanov and D. Porras, Adiabatic quantum metrology with strongly correlated quantum optical systems, *Phys. Rev. A* **88**, 023803 (2013).
- [6] M. Bina, I. Amelio, and M. G. A. Paris, Dicke coupling by feasible local measurements at the superradiant quantum phase transition, *Phys. Rev. E* **93**, 052118 (2016).
- [7] K. Macieszczak, M. Gută, I. Lesanovsky, and J. P. Garrahan, Dynamical phase transitions as a resource for quantum enhanced metrology, *Phys. Rev. A* **93**, 022103 (2016).
- [8] I. Frerot and T. Roscilde, Quantum critical metrology, *Phys. Rev. Lett.* **121**, 020402 (2018).
- [9] S. S. Mirkhalaf, E. Witkowska, and L. Lepori, Supersensitive quantum sensor based on criticality in an antiferromagnetic spinor condensate, *Phys. Rev. A* **101**, 043609 (2020).
- [10] V. Montenegro, U. Mishra, and A. Bayat, Global sensing and its impact for quantum many-body probes with criticality, *Phys. Rev. Lett.* **126**, 200501 (2021).
- [11] A. Niezgoda and J. Chwedeńczuk, Many-body nonlocality as a resource for quantum-enhanced metrology, *Phys. Rev. Lett.* **126**, 210506 (2021).
- [12] G. Di Fresco, B. Spagnolo, D. Valenti, and A. Carollo, Multiparameter quantum critical metrology, *SciPost Phys.* **13**, 077 (2022).
- [13] G. Di Fresco, B. Spagnolo, D. Valenti, and A. Carollo, Metrology and multipartite entanglement in measurement-induced phase transition, *Quantum* **8**, 1326 (2024).
- [14] R. Salvia, M. Mehboudi, and M. Perarnau-Llobet, Critical quantum metrology assisted by real-time feedback control, *Phys. Rev. Lett.* **130**, 240803 (2023).
- [15] A. Sahoo, U. Mishra, and D. Rakshit, Localization-driven quantum sensing, *Phys. Rev. A* **109**, L030601 (2024).
- [16] M. M. Rams, P. Sierant, O. Dutta, P. Horodecki, and J. Zakrzewski, At the Limits of Criticality-Based Quantum Metrology: Apparent Super-Heisenberg Scaling Revisited, *Phys. Rev. X* **8**, 021022 (2018).
- [17] D.-S. Ding, Z.-K. Liu, B.-S. Shi, G.-C. Guo, K. Mølmer, and C. S. Adams, Enhanced metrology at the critical point of a many-body Rydberg atomic system, *Nat. Phys.* **18**, 1447 (2022).
- [18] R. Liu, Y. Chen, M. Jiang, X. Yang, Z. Wu, Y. Li, H. Yuan, X. Peng, and J. Du, Experimental critical quantum metrology with the Heisenberg scaling, *npj Quantum Inf.* **7**, 170 (2021).
- [19] A. Blais, A. L. Grimsmo, S. M. Girvin, and A. Wallraff, Circuit quantum electrodynamics, *Rev. Mod. Phys.* **93**, 025005 (2021).
- [20] J. Clarke, Advances in squid magnetometers, *IEEE Transactions on Electron Devices* **27**, 1896–1908 (1980).
- [21] R. C. Jaklevic, J. Lambe, A. H. Silver, and J. E. Mercereau, Quantum interference effects in josephson tunneling, *Physical Review Letters* **12**, 159–160 (1964).
- [22] S. Danilin and M. Weides, *Quantum sensing with superconducting circuits* (2021).
- [23] T. Hönigl-Decrinis, R. Shaikhaidarov, S. de Graaf, V. Antonov, and O. Astafiev, Two-level system as a quantum sensor for absolute calibration of power, *Physical Review Applied* **13**, 10.1103/physrevapplied.13.024066 (2020).
- [24] D. I. Schuster, A. A. Houck, J. A. Schreier, A. Wallraff, J. M. Gambetta, A. Blais, L. Frunzio, J. Majer, B. Johnson, M. H. Devoret, S. M. Girvin, and R. J. Schoelkopf, Resolving photon number states in a superconducting circuit, *Nature* **445**, 515–518 (2007).
- [25] S. Wolski, D. Lachance-Quirion, Y. Tabuchi, S. Kono, A. Noguchi, K. Usami, and Y. Nakamura, Dissipation-based quantum sensing of magnons with a superconducting qubit, *Physical Review Letters* **125**, 10.1103/physrevlett.125.117701 (2020).
- [26] D. Lachance-Quirion, S. P. Wolski, Y. Tabuchi, S. Kono, K. Usami, and Y. Nakamura, Entanglement-based single-shot detection of a single magnon with a superconducting qubit, *Science* **367**, 425–428 (2020).
- [27] A. V. Dixit, S. Chakram, K. He, A. Agrawal, R. K. Naik, D. I. Schuster, and A. Chou, Searching for dark matter with a superconducting qubit, *Physical Review Letters* **126**, 10.1103/physrevlett.126.141302 (2021).
- [28] X. Zhang, E. Kim, D. K. Mark, S. Choi, and O. Painter, A superconducting quantum simulator based on a photonic-bandgap metamaterial, *Science* **379**, 278–283 (2023).
- [29] A. A. Houck, H. E. Türeci, and J. Koch, On-chip quantum simulation with superconducting circuits, *Nature Physics* **8**, 292–299 (2012).
- [30] R. Demkowicz-Dobrzański and L. Maccone, Using entanglement against noise in quantum metrology, *Phys. Rev. Lett.* **113**, 250801 (2014).
- [31] S. Kurdzialek, W. Górecki, F. Albarelli, and R. Demkowicz-Dobrzański, Using adaptiveness and causal superpositions against noise in quantum metrology, *Phys. Rev. Lett.* **131**, 090801 (2023).
- [32] S. Ashhab, Superradiance transition in a system with a single qubit and a single oscillator, *Phys. Rev. A* **87**, 013826 (2013).
- [33] M.-J. Hwang, R. Puebla, and M. B. Plenio, Quantum phase transition and universal dynamics in the Rabi model, *Phys. Rev. Lett.* **115**, 180404 (2015).

- [34] R. Puebla, M.-J. Hwang, J. Casanova, and M. B. Plenio, Probing the dynamics of a superradiant quantum phase transition with a single trapped ion, *Phys. Rev. Lett.* **118**, 073001 (2017).
- [35] J. Peng, E. Rico, J. Zhong, E. Solano, and I. L. Egusquiza, Unified superradiant phase transitions, *Phys. Rev. A* **100**, 063820 (2019).
- [36] S. Felicetti and A. Le Boit  , Universal spectral features of ultrastrongly coupled systems, *Phys. Rev. Lett.* **124**, 040404 (2020).
- [37] H.-J. Zhu, K. Xu, G.-F. Zhang, and W.-M. Liu, Finite-Component Multicriticality at the Superradiant Quantum Phase Transition, *Phys. Rev. Lett.* **125**, 050402 (2020).
- [38] L. Garbe, M. Bina, A. Keller, M. G. A. Paris, and S. Felicetti, Critical quantum metrology with a finite-component quantum phase transition, *Phys. Rev. Lett.* **124**, 120504 (2020).
- [39] Y. Chu, S. Zhang, B. Yu, and J. Cai, Dynamic framework for criticality-enhanced quantum sensing, *Phys. Rev. Lett.* **126**, 010502 (2021).
- [40] L. Garbe, O. Abah, S. Felicetti, and P. Puebla, Critical quantum metrology with fully-connected models: from Heisenberg to Kibble-Zurek scaling, *Quantum Sci. Technol.* **7**, 035010 (2022).
- [41] K. Gietka, L. Ruks, and T. Busch, Understanding and improving critical metrology: quenching superradiant light-matter systems beyond the critical point, *Quantum* **6**, 700 (2022).
- [42] K. Gietka, Squeezing by critical speeding up: Applications in quantum metrology, *Phys. Rev. A* **105**, 042620 (2022).
- [43] L. Garbe, O. Abah, S. Felicetti, and R. Puebla, Exponential time-scaling of estimation precision by reaching a quantum critical point, *Phys. Rev. Res.* **4**, 043061 (2022).
- [44] T. Ilias, D. Yang, S. F. Huelga, and M. B. Plenio, Criticality-enhanced quantum sensing via continuous measurement, *PRX Quantum* **3**, 010354 (2022).
- [45] D. Yang, S. F. Huelga, and M. B. Plenio, Efficient information retrieval for sensing via continuous measurement, *Phys. Rev. X* **13**, 031012 (2023).
- [46] U. Alushi, W. G  recki, S. Felicetti, and R. Di Candia, Optimality and noise resilience of critical quantum sensing, *Phys. Rev. Lett.* **133**, 040801 (2024).
- [47] M.-L. Cai, Z.-D. Liu, W.-D. Zhao, Y.-K. Wu, Q.-X. Mei, Y. Jiang, L. He, X. Zhang, Z.-C. Zhou, and L.-M. Duan, Observation of a quantum phase transition in the quantum Rabi model with a single trapped ion, *Nat. Commun.* **12**, 1126 (2021).
- [48] A. Delteil, T. Fink, A. Schade, S. H  fling, C. Schneider, and A. Imamo  lu, Towards polariton blockade of confined exciton-polaritons, *Nat. Mat.* **18**, 219 (2019).
- [49] Z. Li, F. Claude, T. Boulier, E. Giacobino, Q. Glorieux, A. Bramati, and C. Ciuti, Dissipative phase transition with driving-controlled spatial dimension and diffusive boundary conditions, *Phys. Rev. Lett.* **128**, 093601 (2022).
- [50] J. M. Fink, A. Dombi, A. Vukics, A. Wallraff, and P. Domokos, Observation of the photon-blockade breakdown phase transition, *Phys. Rev. X* **7**, 011012 (2017).
- [51] P. Brookes, G. Tancredi, A. D. Patterson, J. Rahamim, M. Esposito, T. K. Mavrogordatos, P. J. Leek, E. Ginossar, and M. H. Szymanska, Critical slowing down in circuit quantum electrodynamics, *Science Advances* **7**, eabe9492 (2021).
- [52] Q.-M. Chen, M. Fischer, Y. Nojiri, M. Renger, E. Xie, M. Partanen, S. Pogorzalek, K. G. Fedorov, A. Marx, F. Deppe, *et al.*, Quantum behavior of the Duffing oscillator at the dissipative phase transition, *Nat. Commun.* **14**, 2896 (2023).
- [53] R. Sett, F. Hassani, D. Phan, S. Barzanjeh, A. Vukics, and J. M. Fink, Emergent macroscopic bistability induced by a single superconducting qubit, *PRX Quantum* **5**, 010327 (2024).
- [54] R. Rota, F. Minganti, C. Ciuti, and V. Savona, Quantum critical regime in a quadratically driven nonlinear photonic lattice, *Phys. Rev. Lett.* **122**, 110405 (2019).
- [55] J. Jin, D. Rossini, R. Fazio, M. Leib, and M. J. Hartmann, Photon solid phases in driven arrays of nonlinearly coupled cavities, *Phys. Rev. Lett.* **110**, 163605 (2013).
- [56] T. E. Lee, S. Gopalakrishnan, and M. D. Lukin, Unconventional magnetism via optical pumping of interacting spin systems, *Phys. Rev. Lett.* **110**, 257204 (2013).
- [57] F. Vicentini, F. Minganti, R. Rota, G. Orso, and C. Ciuti, Critical slowing down in driven-dissipative Bose-Hubbard lattices, *Phys. Rev. A* **97**, 013853 (2018).
- [58] M. Foss-Feig, P. Niroula, J. T. Young, M. Hafezi, A. V. Gorshkov, R. M. Wilson, and M. F. Maghrebi, Emergent equilibrium in many-body optical bistability, *Phys. Rev. A* **95**, 043826 (2017).
- [59] W. Casteels, F. Storme, A. Le Boit  , and C. Ciuti, Power laws in the dynamic hysteresis of quantum nonlinear photonic resonators, *Phys. Rev. A* **93**, 033824 (2016).
- [60] N. Bartolo, F. Minganti, W. Casteels, and C. Ciuti, Exact steady state of a Kerr resonator with one- and two-photon driving and dissipation: Controllable wigner-function multimodality and dissipative phase transitions, *Phys. Rev. A* **94**, 033841 (2016).
- [61] H. J. Carmichael, Breakdown of photon blockade: A dissipative quantum phase transition in zero dimensions, *Phys. Rev. X* **5**, 031028 (2015).
- [62] W. Casteels, R. Fazio, and C. Ciuti, Critical dynamical properties of a first-order dissipative phase transition, *Phys. Rev. A* **95**, 012128 (2017).
- [63] Q.-M. Chen, M. Fischer, Y. Nojiri, M. Renger, E. Xie, M. Partanen, S. Pogorzalek, K. G. Fedorov, A. Marx, F. Deppe, *et al.*, Quantum behavior of the duffing oscillator at the dissipative phase transition, *Nat. Commun.* **14**, 2896 (2023).
- [64] T. Fink, A. Schade, S. H  fling, C. Schneider, and A. Imamo  lu, Signatures of a dissipative phase transition in photon correlation measurements, *Nat. Phys.* **14**, 365 (2018).

- [65] F. Minganti, A. Biella, N. Bartolo, and C. Ciuti, Spectral theory of liouvillians for dissipative phase transitions, *Phys. Rev. A* **98**, 042118 (2018).
- [66] G. Beaulieu, F. Minganti, S. Frasca, V. Savona, S. Felicetti, R. Di Candia, and P. Scarlino, *Observation of first- and second-order dissipative phase transitions in a two-photon driven kerr resonator* (2023), arXiv:2310.13636 [quant-ph].
- [67] C. Berdou, A. Murani, U. Réglade, W. Smith, M. Villiers, J. Palomo, M. Rosticher, A. Denis, P. Morfin, M. Delbecq, T. Kontos, N. Pankratova, F. Rautschke, T. Peronnin, L.-A. Sellem, P. Rouchon, A. Sarlette, M. Mirrahimi, P. Campagne-Ibarcq, S. Jezouin, R. Lescanne, and Z. Leghtas, One hundred second bit-flip time in a two-photon dissipative oscillator, *PRX Quantum* **4**, 020350 (2023).
- [68] T. Yamamoto, K. Inomata, M. Watanabe, K. Matsuba, T. Miyazaki, W. D. Oliver, Y. Nakamura, and J. S. Tsai, Flux-driven Josephson parametric amplifier, *Appl. Phys. Lett.* **93**, 042510 (2008).
- [69] H. Puterman, K. Noh, C. T. Hann, G. S. MacCabe, S. Aghaeimeibodi, R. N. Patel, M. Lee, W. M. Jones, H. Moradinejad, R. Rodriguez, *et al.*, Hardware-efficient quantum error correction using concatenated bosonic qubits, arXiv preprint arXiv:2409.13025 (2024).
- [70] U. Réglade, A. Bocquet, R. Gautier, J. Cohen, A. Marquet, E. Albertinale, N. Pankratova, M. Hallén, F. Rautschke, L.-A. Sellem, P. Rouchon, A. Sarlette, M. Mirrahimi, P. Campagne-Ibarcq, R. Lescanne, S. Jezouin, and Z. Leghtas, Quantum control of a cat qubit with bit-flip times exceeding ten seconds, *Nature* **629**, 778–783 (2024).
- [71] S. Fernández-Lorenzo and D. Porras, Quantum sensing close to a dissipative phase transition: Symmetry breaking and criticality as metrological resources, *Phys. Rev. A* **96**, 013817 (2017).
- [72] P. A. Ivanov, Enhanced two-parameter phase-space-displacement estimation close to a dissipative phase transition, *Phys. Rev. A* **102**, 052611 (2020).
- [73] R. Di Candia, F. Minganti, K. Petrovnin, G. Paraoanu, and S. Felicetti, Critical parametric quantum sensing, *npj Quantum Inf.* **9**, 23 (2023).
- [74] A. Cabot, F. Carollo, and I. Lesanovsky, Continuous sensing and parameter estimation with the boundary time crystal, *Phys. Rev. Lett.* **132**, 050801 (2024).
- [75] U. Alushi, A. Coppo, V. Brosco, R. D. Candia, and S. Felicetti, *Collective quantum enhancement in critical quantum sensing* (2024), arXiv:2407.18055 [quant-ph].
- [76] Here,  $\delta$  includes all frequency drifts from nonlinear elements and coupling to external degrees of freedom, representing the detuning between the pump and measured frequency of the cavity, rather than the “bare” resonator frequency. Also notice the convention of calling the detuning  $\omega$ , as the symbol  $\Delta$  is used to indicate errors.
- [77] C. M. Wilson, T. Duty, M. Sandberg, F. Persson, V. Shumeiko, and P. Delsing, Photon generation in an electromagnetic cavity with a time-dependent boundary, *Phys. Rev. Lett.* **105**, 233907 (2010).
- [78] P. Krantz, Y. Reshitnyk, W. Wustmann, J. Bylander, S. Gustavsson, W. D. Oliver, T. Duty, V. Shumeiko, and P. Delsing, Investigation of nonlinear effects in Josephson parametric oscillators used in circuit quantum electrodynamics, *New J. Phys.* **15**, 105002 (2013).
- [79] Z. Lin, K. Inomata, K. Koshino, W. Oliver, Y. Nakamura, J.-S. Tsai, and T. Yamamoto, Josephson parametric phase-locked oscillator and its application to dispersive readout of superconducting qubits, *Nat. Commun.* **5**, 4480 (2014).
- [80] G. Beaulieu, F. Minganti, S. Frasca, V. Savona, S. Felicetti, R. Di Candia, and P. Scarlino, *Observation of first- and second-order dissipative phase transitions in a two-photon driven Kerr resonator* (2023), arXiv:2310.13636 [quant-ph].
- [81] M. Wallquist, V. S. Shumeiko, and G. Wendin, Selective coupling of superconducting charge qubits mediated by a tunable stripline cavity, *Phys. Rev. B* **74**, 224506 (2006).
- [82] C. Eichler and A. Wallraff, Controlling the dynamic range of a Josephson parametric amplifier, *EPJ Quantum Technology* **1**, 2 (2014).
- [83] S. Probst, F. B. Song, P. A. Bushev, A. V. Ustinov, and M. Weides, Efficient and robust analysis of complex scattering data under noise in microwave resonators, *Review of Scientific Instruments* **86**, 024706 (2015).